remote sensing

MDPI

Article

Projecting Climate and Land Use Change Impacts on Actual Evapotranspiration for the Narmada River Basin in Central India in the Future

Sananda Kundu [1], Arun Mondal [1], Deepak Khare [2], Christopher Hain [3] and Venkat Lakshmi [1,*]

[1] School of Earth, Ocean and the Environment, University of South Carolina, Columbia, SC 29208, USA; skundu@geol.sc.edu (S.K.); amondal@geol.sc.edu (A.M.)
[2] Department of Water Resources Development and Management, Indian Institute of Technology Roorkee, Roorkee, Uttarakhand 247667, India; kharefwt@gmail.com
[3] NASA Marshall Space Flight Center, Earth Science Branch, Huntsville, AL 35805, USA; christopher.hain@nasa.gov
* Correspondence: vlakshmi@geol.sc.edu

Received: 20 February 2018; Accepted: 5 April 2018; Published: 9 April 2018

check for updates

Abstract: Assessment of actual evapotranspiration (ET) is essential as it controls the exchange of water and heat energy between the atmosphere and land surface. ET also influences the available water resources and assists in the crop water assessment in agricultural areas. This study involves the assessment of spatial distribution of seasonal and annual ET using Surface Energy Balance Algorithm for Land (SEBAL) and provides an estimation of future changes in ET due to land use and climate change for a portion of the Narmada river basin in Central India. Climate change effects on future ET are assessed using the ACCESS1-0 model of CMIP5. A Markov Chain model estimated future land use based on the probability of changes in the past. The ET analysis is carried out for the years 2009–2011. The results indicate variation in the seasonal ET with the changed land use. High ET is observed over forest areas and crop lands, but ET decreases over crop lands after harvest. The overall annual ET is high over water bodies and forest areas. ET is high in the premonsoon season over the water bodies and decreases in the winter. Future ET in the 2020s, 2030s, 2040s, and 2050s is shown with respect to land use and climate changes that project a gradual decrease due to the constant removal of the forest areas. The lowest ET is projected in 2050. Individual impact of land use change projects decreases in ET from 1990 to 2050, while climate change effect projects increases in ET in the future due to rises in temperature. However, the combined impacts of land use and climate changes indicate a decrease in ET in the future.

Keywords: actual ET; SEBAL; land use change; Markov Chain model; climate change; CMIP5; Central India

1. Introduction

The estimation of actual evapotranspiration (ET) and its spatial distribution over a large area are considered an extremely important variable in the efficient management of water resources and agriculture. In addition, ET is considered one of the major components of the hydrological cycle, apart from the rainfall and runoff. It is affected at the interface of vegetation, soil, and atmosphere by atmospheric, soil, and biophysical processes [1]. A global shortage of water resources affects agricultural productivity [2]. According to Gowda et al. [3], reliable estimation of ET is required to improve the water use efficiency. Both climate and land use are key components in ET and water use efficiency. Climate change is causing a global rise in mean temperature, which is projected to increase 0.8–2.6 °C on average by 2050 [4]. A rise in temperature will cause an increase in ET, further impacting already limited water resources. Land use is also expected to change by 2050. ET plays an important role in the atmospheric processes since it controls the water supply from the ocean and earth's surface to the atmosphere. It also influences the spatial distribution and magnitude of global temperature and pressure [5], and the incidence of heat waves [6]. The actual ET is the water quantity, which is transferred to the atmosphere as water vapor from an evaporating surface under actual conditions (vegetation type, climate, physiological mechanisms, water availability) [7,8]. Climate change is an important factor that influences the watershed hydrology and water availability of plants by different patterns of ET and rainfall [9,10]. ET determines climate drought in arid and semi-arid areas, and changes in meteorological variables due to climate affect crop water requirements [11,12].

Precise measurement of actual ET is possible using instruments such as lysimeters [13] and eddy covariance measurements [14]. However, these methods are not always easy to implement and are expensive [13], and do not give an estimation over large areas like satellite data. ET is an important part of the hydrological and climate cycles, with substantial ecological, agricultural, and hydrological implications [7,15]. The ET computation by remote sensing is mostly based on the energy balance from satellite sensors [16–18]. Many studies have used an energy balance methodology for computing the net radiation, sensible heat flux, and soil heat flux, which can be used to estimate actual ET [19,20]. Since the energy balance and the crop water stress are directly related to the water use in agriculture, the differences in actual ET in space and time are generally considered to be a major indicator for deciding the reliability and adequacy of the irrigation and equitable water use. ET obtained from remote sensing relates the water balance to the surface energy balance and the landscape heterogeneity. There has been recent progress in the availability of fine to medium resolution images that have increased the prospective application. The Moderate-Resolution Imaging Spectroradiometer (MODIS) of medium resolution vegetation products, can derive physical parameters at the basin scale for surface energy balance models [21–24]. MODIS has been used in different studies to estimate ET from surface energy balance [25–27]. The Surface Energy Balance Algorithm for Land (SEBAL; [28,29]) is a validated and widely-used, remote-sensing-based model for estimating ET [13,24,30–33]. This model can be implemented by using the thermal band of satellite sensors and various weather parameters such as solar radiation, air temperature, wind speed, and humidity [33]. In the SEBAL method, the requirement of minimum information or a small quantity of ground-based inputs for the computation of actual ET at each pixel and its ability to estimate over large areas [34] is a major advantage where ground measurements are not available. SEBAL considers a linear relationship between land surface temperature (LST) and near-surface vertical temperature gradient which is decided by extreme cold and extreme hot pixels [6,19].

Various studies focused on ET validation from the SEBAL model in different parts of the world like in India, Spain, Italy, Sri Lanka, China, Pakistan, and Iran [13,29,35]. Satisfactory results are observed in the works of Ahmad et al. [36] in the Krishna river basin of India, Sun et al. [30] and Du et al. [31] in northeast China, and Bashir et al. [34] in Sudan. In India, the performance of SEBAL-based ET was tested against the lysimeter ET on an agricultural farm located in a humid region and shows good accuracy of the model-generated ET [37]. In the subtropical to semi-arid region of Gujrat [38] and the semi-dry-humid region of Dehradun [39], SEBAL-based ET was used to estimate the crop water requirement to assess the performance of the canal irrigation system. In another study, the Simplified Surface Energy Balance (SSEB) was used in the IndoGangetic Basin for mapping rice water consumption, yield, and water productivity [40]. Monthly actual ET is measured in Saudi Arabia using SEBAL and is applied on the irrigated croplands [41]. The SEBAL model has been applied mainly in agricultural areas [17,35,41–47], including to study flood mitigation in irrigation development or to investigate water availability and use [48,49]. Studies with SEBAL also concentrate on a specific land use type in some cases [50]. Some recent studies involve comparisons of various energy balance methods such as SEBAL, SEBS (Surface Energy Balance System), SSEB (Simplified Surface Energy Balance) and METRIC (Mapping Evapotranspiration at high Resolution with Internalized Calibration) [51–53]. Other perspectives of the studies involve the impact of the resolution of satellite images, variation in the scale or investigation, and coupling of different methodologies and their accuracy in estimating actual ET [41,54–58]. All the previous and recent literature discussed above shows various types of applications and methodologies to estimate actual ET with or without SEBAL in different parts of the world. However, estimation of the effects of land use and climate changes on future actual evapotranspiration has never been assessed before.

The main objective of the present research is to estimate and assess the spatial distribution of ET over the basin study area for three consecutive years (2009–2011) on a seasonal and annual basis and to assess the impact of present and future land use changes and future climate changes on actual ET. This work includes subobjectives of: (1) estimation of ET using SEBAL and assessing the spatial distribution over the study area on an annual and seasonal basis; (2) assessment of land use change effects on future ET; (3) assessment of climate change effects on future ET; and (4) combined effects of climate and land use changes on ET.

2. Study Area

The study area is a part of the Narmada river basin in Madhya Pradesh of Central India and the area extends from 21°47′24″ to 23°26′06″N latitude and 77°34′44″ to 78°42′21″E longitude. The total basin area is 12,290 km^2 between gauge stations of Hoshangabad and Sandia. Monsoon season is considered a unique feature of this area and of India and is the highest source of rain water (80%). Premonsoon or summer season is from March to May; monsoon season extends from June to September; postmonsoon season is in October and November; and winter extends from December to February. The annual average rainfall varies from 900 to 1150 mm, and annual minimum and maximum temperatures vary from 19.5 to 32.5 °C, as noticed in 41 years of data (1971–2011). Clay and clay loam soils cover more than 50% of the study area. Other types of soils observed in the area are sandy clay loam, sandy loam, and sandy clay. The elevation is highest in the southwest and south, and medium to low in the north. Plain lands with low elevation are found mostly in the north central part, and the elevation of the entire area ranges from 232 to 1312 m (Figure 1).

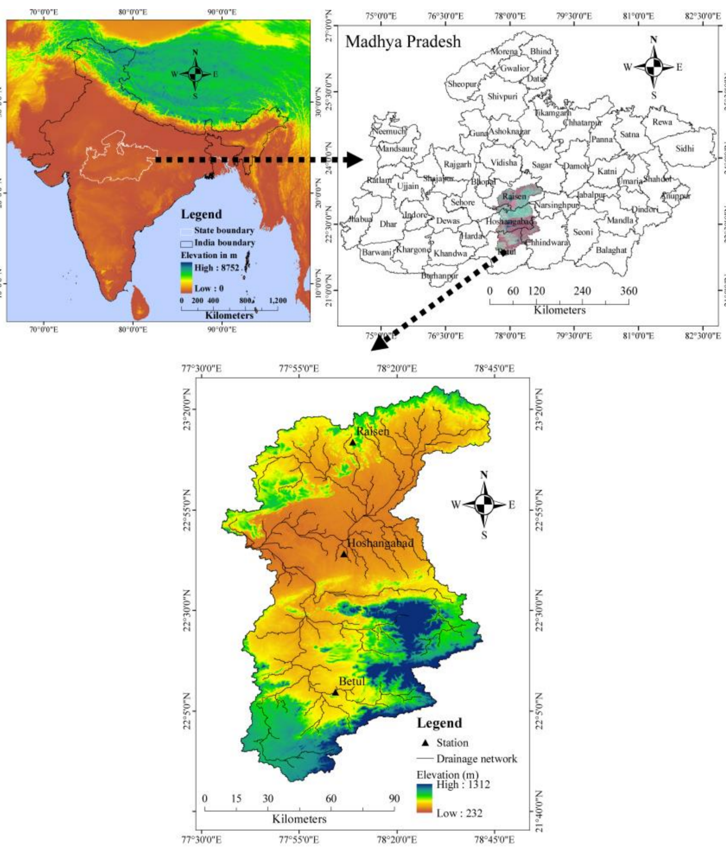

Figure 1. Location, elevation, and drainage network of the study area.

3. Data and Methodology

The details of the data used in this paper are listed in Table 1. The study area has three observed weather station data from the India Meteorological Department (IMD), which were used in the study. These stations are Hoshangabad, Raisen, and Betul.

Table 1. Data used for the study.

Data Input	Source
Temperature (°C) Relative Humidity (%) Wind speed (m/s) Incoming solar radiation (W/m^2)	Indian Meteorological Department (IMD)
Satellite Data Input (MODIS)	USGS
Temperature (°C) (Climate change analysis)	CORDEX

The methodology followed in the estimation of ET and impact in the future due to climate and land use changes are described below:

(i) ET was generated using SEBAL with 3 years (2009–2011) of MODIS data, and an average of three years of data was considered to reduce the uncertainty in actual ET estimation. Cloud-free images of 8-day composite were used to give the seasonal (premonsoon, monsoon, postmonsoon, and winter) and annual ET of three years.

(ii) Land use classification into 10 classes was done using Maximum Likelihood Classification techniques with three images from 1990, 2000, and 2011. The land use change prediction of 2020, 2030, 2040, and 2050 was done with the Markov Chain model using data from 1990, 2000, and 2011.

(iii) To estimate climate change, RCP data from two scenarios (4.5 and 8.5) were used. Change in the minimum and maximum temperatures in the past and future was estimated by taking an average of 10 years of data. Climate change assessment of different decades spans the 1990s (average of 1986–1995), 2000s (1996–2005), 2011s (2006–2015), 2020s (2016–2025), 2030s (2026–2035), 2040s (2036–2045), and 2050s (2046–2055).

(iv) The mean ET for 10 different land use classes was estimated from the 3 years' mean ET of different seasons (2009–2011). The mean ET thus obtained was taken as a constant for different land use classes. The impact of land use change on ET was done by taking mean ET of 10 land use classes as constants on the basis of 2011 land use, and estimating ET of the past (1990, 2000) and future (2020, 2030, 2040, and 2050) with respect to changed land use by areal average method.

(v) The impact of climate change on ET in all the years was estimated by changing the minimum and maximum temperature of the corresponding years (1990s, 2000s, 2020s, 2030s, 2040s, and 2050s) in the SEBAL model. All other parameters were kept constant (of the years 2009–2011). ET changes due to the effect of climate change for each decade were obtained by averaging ET of three years (2009–2011).

(vi) (The mean ET of 10 land use classes of each decade (of climate years) was estimated on the basis of 2011 land use. Estimation of the combined impact of land use and climate change on future ET was done by using these mean ET (1990s, 2000s, 2011s, 2020s, 2030s, 2040s, 2050s) with the corresponding land use areas (1990, 2000, 2011, 2020, 2030, 2040, 2050) by areal average method (Figure 2A).

Details of the models used in the study are described in the following paragraphs.

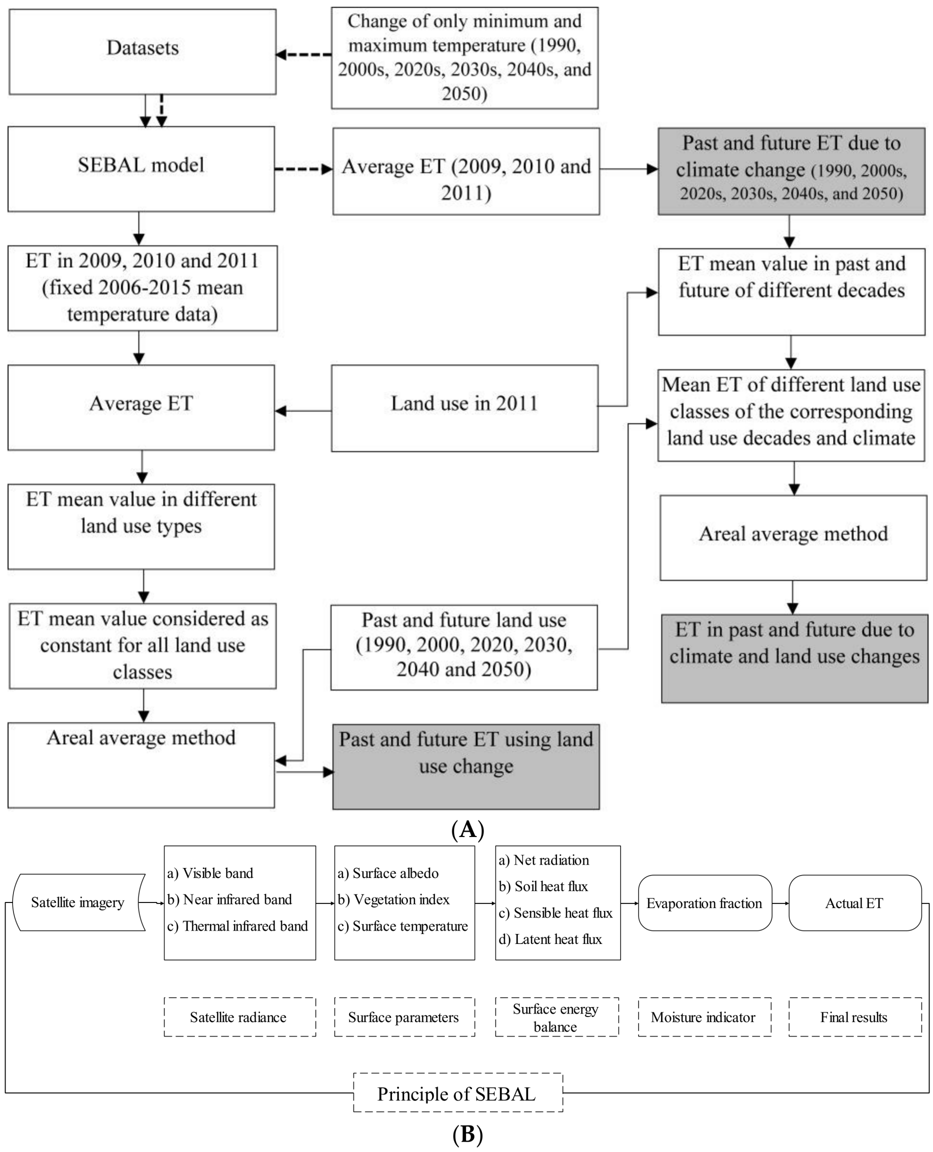

Figure 2. (**A**) Process of future land use and climate change on future actual ET; (**B**) Principle of the SEBAL model.

3.1. SEBAL Model (Actual ET)

Also, to estimate actual ET, Level 3 LST and surface reflectance data of MODIS of 2009–2011 were utilized, which were retrieved from the Terra satellite and were being distributed by the United States Geological Survey (USGS). The MOD11A2 [50] data product of MODIS (8-day composite) was used for LST and emissivity, which has 1 km of resolution. Surface albedo was used from the product MCD43B3 which was retrieved by the MODIS sensors from the Terra satellites [11] with 16-day temporal and 1-km spatial resolution. Surface reflectance was obtained from the MODIS product of MOD09Q1 [9], which is an 8-day composite product and has the spatial resolution of 250 m. The NDVI was calculated from the surface reflectance, which is a MODIS product.

In SEBAL, the ratio of soil heat flux (G) and net radiation flux (Rn) i.e., G/Rn was calculated by Bastiaanssen [42]. Net radiation (Rn) was calculated using shortwave radiation, surface albedo, longwave radiation, and thermal emissivity. Soil heat flux (G) was calculated using net radiation, surface temperature, surface albedo, and NDVI. Sensible heat flux (H) was calculated from the surface roughness, surface temperature, and wind speed. The visible, near infrared, and thermal bands were used in the SEBAL model as inputs to generate the LST, albedo, and vegetation index which are further used to obtain net radiation, soil heat flux, latent heat flux, and sensible heat flux [28,29]. Finally, actual ET was generated using the evaporative fraction. The surface energy budget equation is [28],

$$ET = Rn - G - H \tag{1}$$

where ET represents the latent heat flux (W/m^2) linked with water evaporation from soil and vegetation, Rn gives the net radiation flux at the surface (W/m^2), G is the soil heat flux (W/m^2), and H stands for the sensible heat flux for the cooling and warming of air (W/m^2). The methodology followed in estimating SEBAL ET is illustrated in Figure 2B.

Computation of other parameters such as the Rn [28], incoming shortwave radiation ($R_{S\downarrow}$, [59]), α or surface albedo, incoming longwave radiation ($R_{L\downarrow}$) and outgoing longwave radiation ($R_{L\uparrow}$, [60]), normalized difference vegetation index (NDVI) and leaf area index (LAI) [61], G, H, latent heat flux (λET), instantaneous ET (ET_{inst}), and reference ET fraction (ET_rF, [42]) were done. Finally, the daily actual ET (ET_{24}) and seasonal actual evapotranspiration ($ET_{seasonal}$) were calculated [62]. The SEBAL algorithm uses two pixels of cold or wet and hot or dry. For e.g., a cold pixel is selected from a well-irrigated land with maximum ET, and a dry pixel from a dry or bare agricultural land where ET is considered as 0 [51]. In this study, the cold pixel was selected from a crop area or an agricultural land and the hot pixel was selected from an open bare land.

3.2. Land Use Classification and Future Projection

The land use classification was done, and prediction was carried out using the Markov Chain model [63–67], where a 2011 classified image was validated with the 2011 predicted image. The Advanced Spaceborne Thermal Emission and Reflection Radiometer Global Digital Elevation Model (ASTER GDEM) [68] was used to obtain elevation information of the study area. The Landsat images of 1990, 2000 (USGS), and 2011 (Linear Imaging Self Scanning Sensor or LISS-III, Indian Remote Sensing Satellite) were used for classification and prediction. 1990, 2000, and 2011 images were projected in the Universal Transverse Mercator projection zone 44 and WGS 84 datum. Radiometric and geometric corrections were done with the Root Mean Square Error (RMSE) of 0.5 pixels in the first order polynomial in geometric correction. The Maximum Likelihood Classification (MLC) [61,62,69,70] was used for classification and the accuracy assessment was done. The Markov Chain model [71] was used in the classified 1990, 2000, and 2011 images to predict future land use of 2020, 2030, 2040, and 2050. Model calibration and validation were conducted using classified 2011 and model-generated 2011 images. The area matrix was used to analyze the changes. The future maps of 2020 to 2050 with changed land use were used to show changes in the future ET. Field surveys were conducted during the summer and winter seasons of 2011 to obtain the location of different land classes for accuracy assessment by GPS.

The Markov Chain model was used for projecting future land use change. The model develops transition matrix and conditional probability images by investigating the land use classes of diverse times and dates. The matrix shows the pixels, which were projected to change from one class to another over a unit of time. It also indicates the probability of change of one class to another class. The land use change is the stochastic process in the Markov Chain model, and various classes exist in a state of a chain. A chain is a stochastic process at time t, where Xt is based on the value at t-1, Xt-1 time. It is not based on such values as Xt-2, Xt-3, . . . , X0, so that the process passed the course in arriving at Xt-1 [71].

3.3. Climate Change Prediction

To estimate the influence of climate change on future ET, maximum and minimum temperature data were obtained from the ACCESS1-0 model of Coupled Model Intercomparison Project Phase 5 (CMIP5) for two (RCP4.5 and RCP8.5) future scenarios [63,72]. Data were obtained from Coordinated

Regional Climate Downscaling Experiment (CORDEX) South Asia models. These data for the South Asia region are distributed by publishing on the CCCR-IITM Climate Data Portal (http://cccr.tropmet.res.in/home/ftp_data.jsp). Daily climate data required for the models were obtained from the India Meteorological Department (IMD).

4. Results

4.1. Seasonal and Annual Land Surface Temperature (LST) and Normalized Difference Vegetation Index (NDVI)

The seasonal LST and NDVI of three years are presented in Figures 3 and 4. In the premonsoon season (March–May), LST is high throughout the study area, varying from 20 to about 53 °C in different years. Low temperature corresponds to the forests. Moderate to high LST is observed over the agricultural area and fallow lands in the north central part. The end of premonsoon or summer season is marked by crop harvest, which results in high LST over agricultural fallow lands. The monsoon (June–September) season is represented by September only due to lack of cloud-free data from June to August. This is the season of maximum rainfall and the LST varies from about 25 to 42 °C. Forest area in the south and north experiences low temperatures, while agricultural fallow lands show high temperatures during crop harvest before September. However, the LST is lower than the premonsoon season. The LST of postmonsoon (October–November) season varies from 23.44 to 37.72 °C. High LST is observed over the fallow agricultural lands, and low LST is observed over the forest and vegetation. The winter season (December–February) marks the crop-growing Rabi (local name for winter crop) season. Therefore, low LST is observed over the agricultural and forest areas in the central part of the study area, and high LST is observed over plain lands and less vegetated areas. Winter LST varies from 20.51 to 33.56 °C.

The NDVI of the premonsoon season varies from −0.17 to 0.61 in different years. High NDVI is observed over the forest and vegetated areas in the south central part. Medium to low NDVI is observed over the agricultural land where most crops are harvested. Low LST is observed over plain and less vegetated areas in the north. The areas of low NDVI also correspond to the areas of high LST. Most of the northern part of the basin show low NDVI, which is mainly agricultural lands and settlements. The NDVI of monsoon season varies from −0.13 to 0.91. The highest NDVI is observed over the forest and vegetated areas while low NDVI is observed over agricultural fallow. The monsoon season leads to the growth of vegetation that has resulted in higher NDVI during September. The NDVI of the postmonsoon season varies from −0.12 to 0.85. The results found high NDVI over forest and vegetation and lowest NDVI over agricultural lands, which are empty of any crop cover during this season. The winter NDVI varies from −0.99 to 0.87 and high NDVI is observed over the agricultural land as this is the season of crop cultivation. Forest areas reflect low NDVI during winter in comparison to agricultural lands.

The vegetation index shows high values when LST is low. Other studies also have indicated such an inverse linear relationship between the NDVI and LST [73–78]. Vegetated lands are cooler than the areas which are not vegetated; therefore, crop areas show higher NDVI, and after crop removal, NDVI decreases. Vegetation canopy with higher leaf area index (LAI) restrains direct surface heating as higher LAI intercepts the incident solar radiation. It also alters the energy flux at the surface because of ET and constant cooling of the surface [21,74].

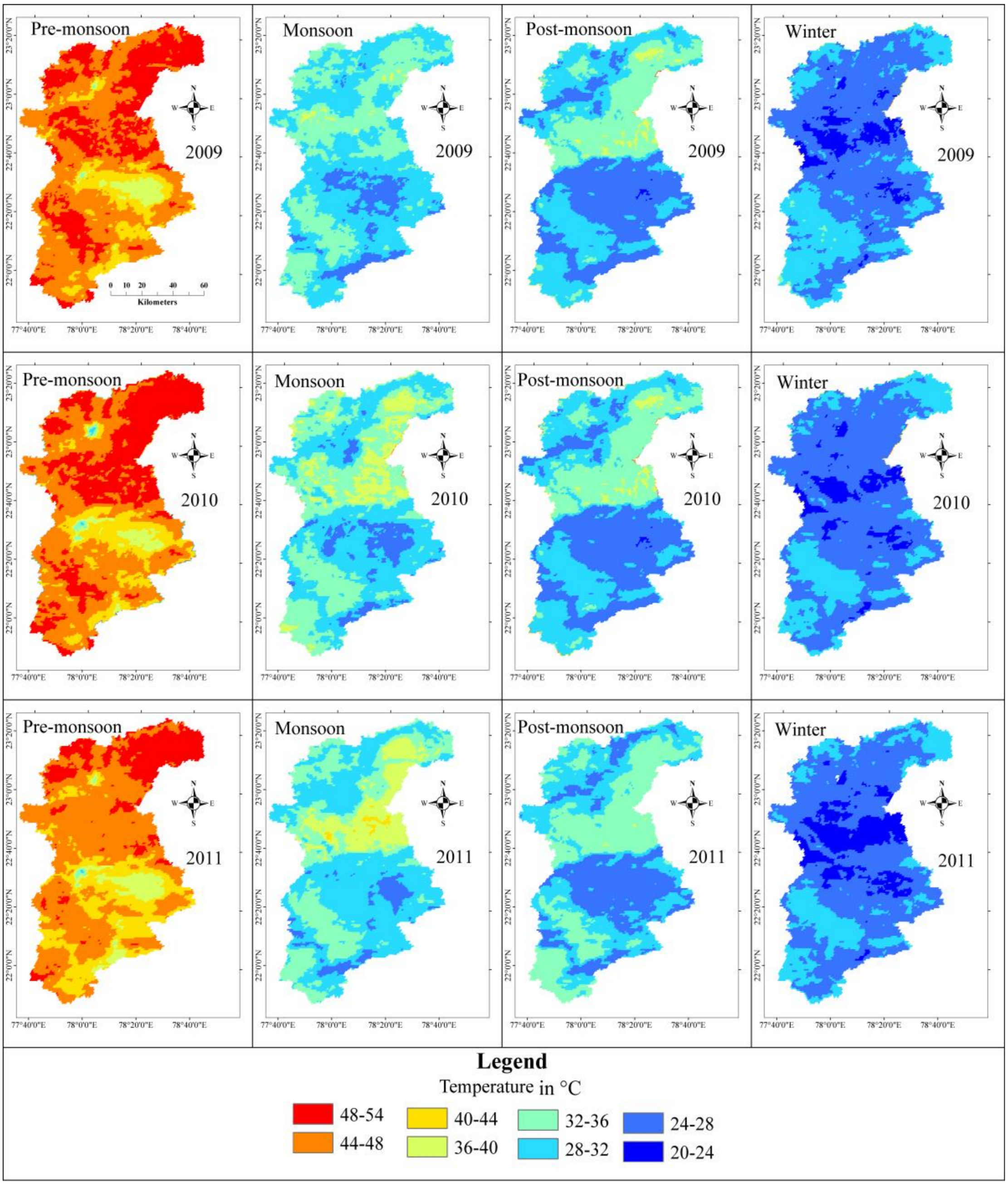

Figure 3. Seasonal land surface temperature (LST) for 2009, 2010, and 2011.

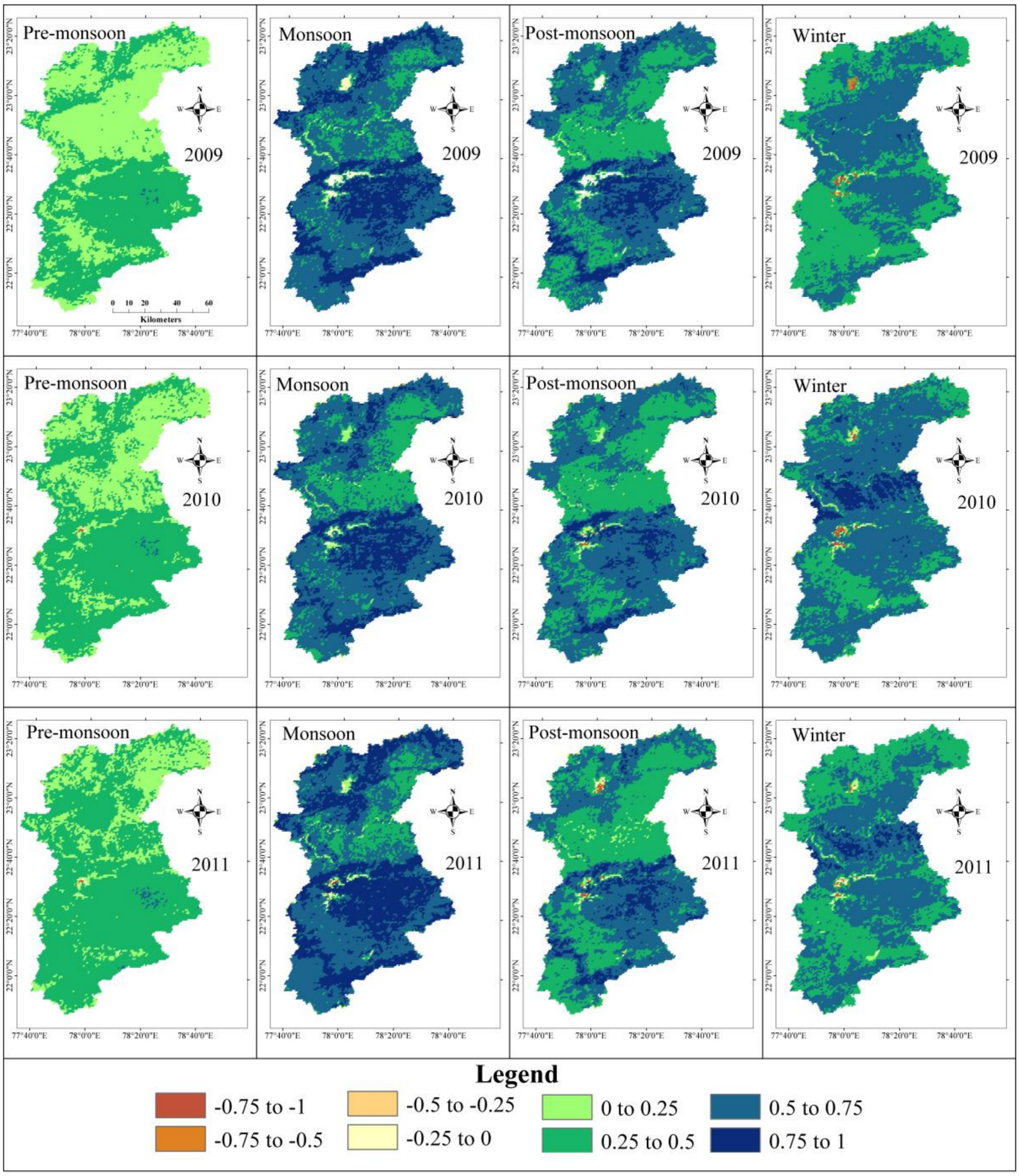

Figure 4. Seasonal normalized difference vegetation index (NDVI) for 2009, 2010, and 2011.

4.2. Seasonal and Annual Actual ET of 2009–2011

The annual and seasonal actual ET (2009–2011) of premonsoon, monsoon, postmonsoon, and winter is given in Figure 5. The seasonal maps show the spatial variation of actual ET annually and for different seasons. In the premonsoon season, ET varies from 154.58 to 646.48 mm. Forest and vegetation in the south and central parts show high ET. The northern part of the basin shows low ET since these are the summer months and crops are harvested from the agricultural fields. The monsoon season is represented by September in this study when crops are already harvested. Therefore, agricultural lands show low ET. The overall ET in monsoon season varies from 49.36 to 489.65 mm. It is lower than premonsoon season because of low surface temperature, rainfall, and overcast skies during this period. Low ET is observed in the agricultural land after crop harvest, and high ET is observed over the water bodies and forest areas. ET in postmonsoon season varies from 43.04 to 243.40 mm. Low

ET is observed over the agricultural land in the north, which are fallow lands. High ET is found in the forest areas. In the winter season, ET ranges from 71.79 to 290.15 mm, and this is a crop-growing season of the year. In all the seasons, NDVI also varies with ET. The crop-growing season of the year corresponds with the ET of different land use. The crop calendar of the study area is given in Table 2.

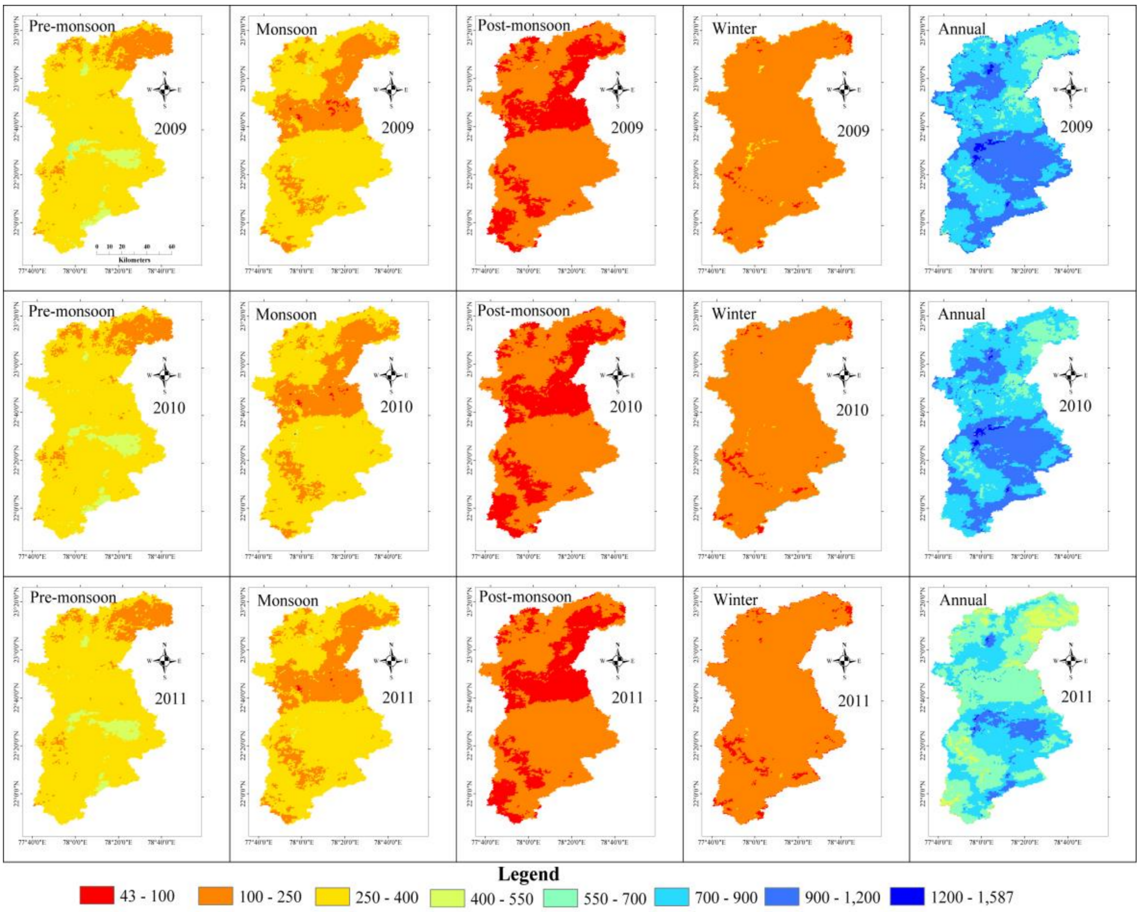

Figure 5. Seasonal and annual actual evapotranspiration (ET in mm) for 2009, 2010, and 2011.

Table 2. Sowing and harvesting season of crops.

Sl. No.	Crops	Month of Sowing	Month of Harvesting
1	Wheat	November–December	February–March
2	Seasonal vegetables	June–July	September–Octorber
3	Seeds	November	February
4	Paddy	June–July	Octorber–November

The annual ET ranges from 318.78 to >1500 mm. The lowest temperature/highest ET corresponds to forested areas and water bodies. Agricultural plain lands indicate moderate to low ET. Areas in the extreme northeast show low ET, which are mostly fallow lands and stony surface areas. The surface temperature in these areas is high with medium to low NDVI. The rocky surface areas, settlements, and fallow lands exhibit higher LST but low NDVI and low ET.

4.3. Future Scenarios of Land Use Change

The impact of land use change on actual ET and seasonal variation is crucial for agricultural management. The past, present, and future land use maps generated with classification technique and

Markov Chain are given in Figures 6 and 7. Areas of different land use classes of 1990, 2000, 2011, 2020, 2030, 2040, and 2050 are given in Table 3.

Table 3. Area of the land use classes of 1990, 2000, and 2011; Area of the land use classes of future by Markov Chain model.

		1990		2000		2011	
Sl. No.	**Classes**	**Area (km^2)**	**Area (%)**	**Area (km^2)**	**Area (%)**	**Area (km^2)**	**Area (%)**
1	Settlement	217.47	1.77	309.39	2.52	386.10	3.14
2	Grassland	1458.37	11.87	1367.25	11.12	1339.76	10.90
3	Forest	3664.04	29.81	3180.16	25.88	2726.56	22.19
4	Scattered	1270.51	10.34	1132.79	9.22	988.14	8.04
5	Agriculture	4106.21	33.41	5010.22	40.77	5643.67	45.92
6	Lake/reservoir	242.15	1.97	245.31	2.00	263.28	2.14
7	River bank	48.68	0.40	30.62	0.25	29.41	0.24
8	Wasteland	1138.95	9.27	855.23	6.96	741.85	6.04
9	River	56.37	0.46	65.62	0.53	63.08	0.51
10	Rocky surface	87.25	0.71	93.40	0.76	108.16	0.88
	Total	12,290	100	12,290	100	12,290	100

		2020		2030		2040		2050	
Sl No.	**Classes**	**Area (km^2)**	**Area (%)**	**Area (km^2)**	**Area (%)**	**Area (km^2)**	**Area (%)**	**Area (km^2)**	**Area (%)**
1	Settlement	484.01	3.94	577.42	4.70	647.47	5.27	710.23	5.78
2	Grassland	1276.43	10.39	1221.12	9.94	1171.96	9.54	1125.65	9.16
3	Forest	2310.91	18.80	1948.36	15.85	1663.23	13.53	1391.62	11.32
4	Scattered	870.26	7.08	728.93	5.93	610.94	4.97	508.01	4.13
5	Agriculture	6275.32	51.06	6848.04	55.72	7305.22	59.44	7755.25	63.10
6	Lake/reservoir	270.51	2.20	284.03	2.31	293.25	2.39	303.50	2.47
7	River bank	21.80	0.18	16.88	0.14	12.58	0.10	10.17	0.08
8	Wasteland	598.54	4.87	462.12	3.76	357.66	2.91	245.20	2.00
9	River	64.23	0.52	70.38	0.57	72.22	0.59	70.23	0.57
10	Rocky surface	117.98	0.96	132.73	1.08	154.85	1.26	170.14	1.38
	Total	12,290	100	12,290	100	12,289	100	12,290	100

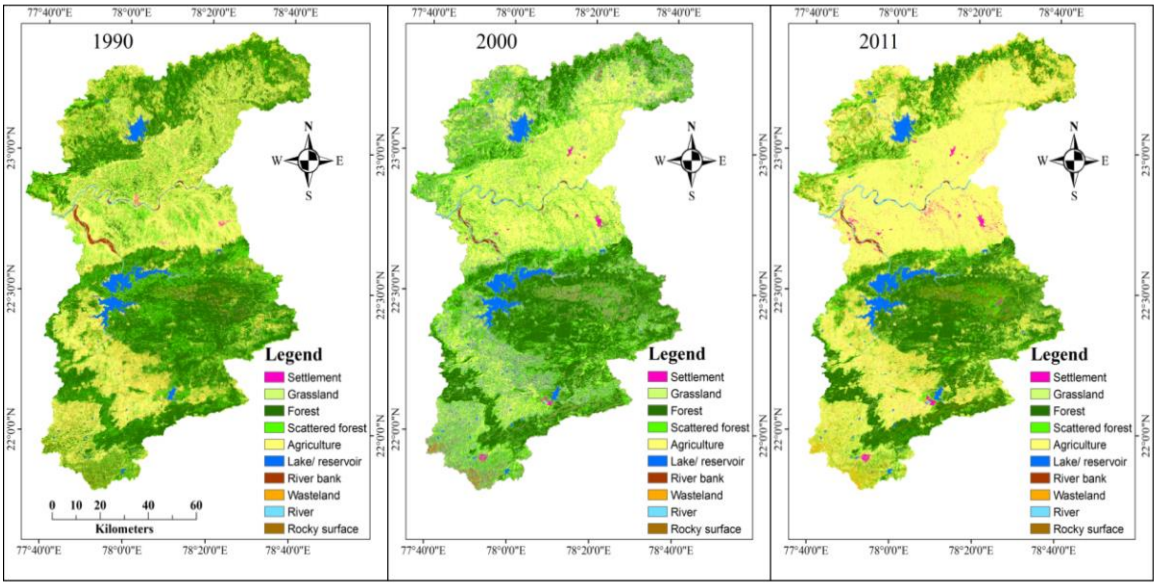

Figure 6. Land use maps of 1990, 2000, and 2011.

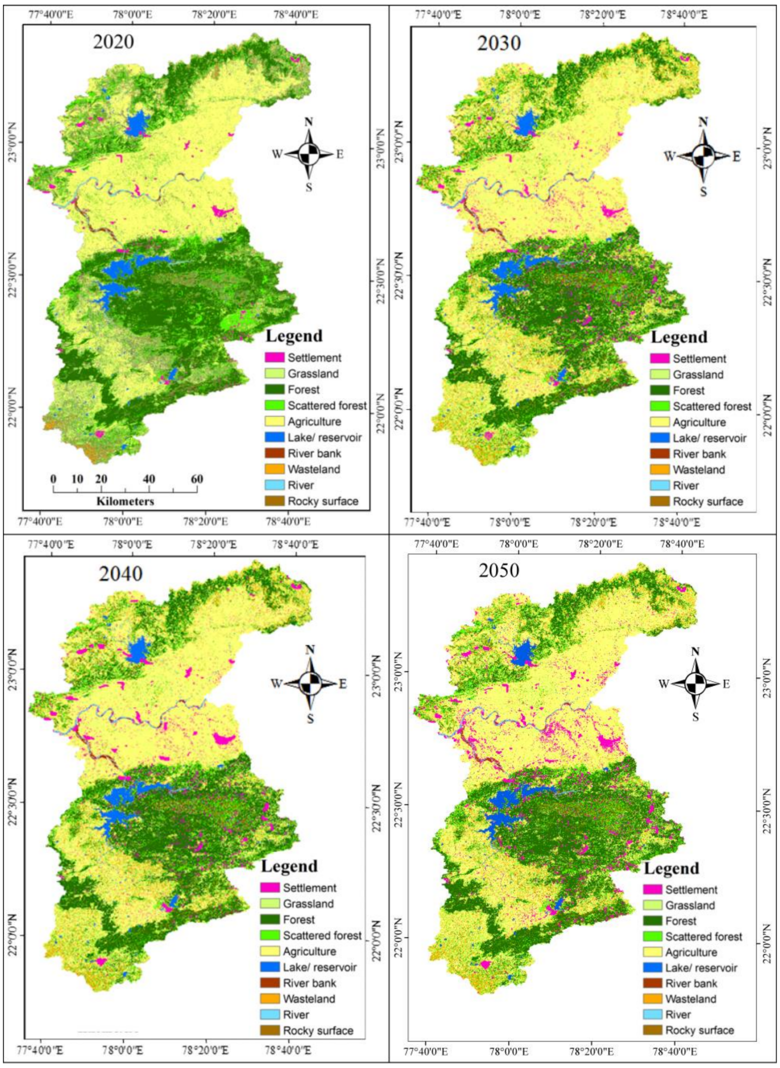

Figure 7. Land use maps of 2020, 2030, 2040 and 2050.

The land use of the study area is classified into 10 major classes such as settlement, agriculture, forest, scattered forest, grassland, river, lake/reservoir, river bank, wasteland, and rocky surface. The 1990 classification shows that 1.77% of the total area is covered by settlements; the maximum area of 33.41% is covered by agricultural land; forest areas cover 29.81%; scattered forest covers 10.34%; grassland covers 11.87%; and wasteland covers 9.27% of the total area. River, lake/reservoir, river bank, and rocky surface cover fewer areas. The agricultural land area is highest, followed by the forest areas. The 2000 land use change shows an increase in the settlement area to 2.52%; agriculture land also increased to 40.77%; grassland covers 11.12% of the area; forest areas decreased to 25.88%; scattered vegetation reduced to 9.22%; grassland reduced to 11.12%; and wasteland area decreased to 6.96%. Therefore, agricultural land and settlements have increased in 2000, while forest, scattered forest, grassland, and wasteland areas have decreased. Hence, there is a transfer of the wasteland and vegetated areas to settlement and agriculture. Change in the 2011 land use shows a further increase in settlement to 3.14% of the area; an increase in agriculture to 45.92% of the area; a decrease in the forest, scattered forest, and grassland areas to 22.19%, 8.04%, and 10.90%, respectively; wasteland areas also decreased to 6.04%; and rocky surface increased to 0.88%. The overall Kappa statistics were 0.82, 0.81, and 0.82, and the overall accuracy was 85%, 84%, and 86% in 1990, 2000, and 2011, respectively. The strength of the accuracy assessment was within the category of almost perfect as it ranges between 0.81 and 0.82 [79].

Increased settlements of 3.94%, 4.70%, 5.27%, and 5.78% are projected in 2020, 2030, 2040, and 2050, respectively. Agriculture area is also estimated to increase to 51.06% in 2020, 55.72% in 2030, 59.44% in 2040, and 63.10% in 2050. The forest area is estimated to decrease at a greater extent to 18.80% in 2020 and 11.32% in 2050; scattered forest areas are also predicted to reduce to 7.08% in 2020 and 4.13% in 2050; and grassland areas to 10.39% in 2020 and 9.16% in 2050. Fewer changes are expected in the river, lake/reservoir, and river bank areas. The wasteland areas are predicted to reduce to 2% in 2050. The rocky surface area shows little change, with a projected increase in the future from 0.88% in 2011 to 1.38% in 2050. Agricultural land and settlements are indicating a continuous increase while the rest of the land use classes are showing decreases at the expense of agriculture and settlement. The land use change prediction by the Markov Chain Model depicts a further decrease in vegetation cover with increasing settlements and agriculture, which may affect future ET.

Seasonal Mean ET for Different Land Use

The averages of seasonal ET for different land use of 2009, 2010, and 2011 are given in Table 4. The highest ET is observed over the water bodies followed by forests, vegetation, and agriculture. Low ET is observed over rocky surfaces followed by wasteland and settlements. Total ET is highest in the water bodies in premonsoon season (647.07 mm) followed by forest (467.77 mm). The lowest is observed over settlement and agricultural fallow in the postmonsoon season. Settlements have shown high ET in the premonsoon or summer season and the lowest ET in the postmonsoon season. Forest areas usually experience high ET throughout the year and the lowest ET in the winter season. Agricultural lands show high mean ET during the premonsoon season and crop growing season in winter, and the lowest is observed in the postmonsoon season. The crop growing season is primarily from November–December to February–March (winter and early premonsoon or summer) and June–July to September (monsoon). River bank areas show a moderate ET value, which is high in the premonsoon season and low in the postmonsoon season. The river banks are generally bare lands and thus indicate low ET. Wasteland areas also depict low ET, with the lowest in winter and the highest in the monsoon season. Rocky surface experiences the lowest ET among all the land use classes, and it is the lowest during the postmonsoon season.

Table 4. Average seasonal ET for different land use (2009–2011) generated from MODIS (mm).

Sl. No	Classes	Settlement	Grassland	Forest	Scattered Forest	Agriculture	Water Body	River Bank	Wasteland	Rocky Surface
1	Premonsoon	294.71	300.02	467.77	331.86	282.39	647.07	346.33	228.52	189.11
2	Monsoon	183.20	257.42	429.03	389.59	159.62	497.96	183.41	315.17	175.88
3	Postmonsoon	78.18	116.05	220.31	199.62	80.52	263.27	99.68	161.70	89.47
4	Winter	191.10	169.00	201.05	159.05	191.70	293.10	150.85	116.40	111.60

4.4. Future Climate Change

The impact of climate change on ET and seasonal variation is applied in the present study. The maximum and minimum temperature of CMIP5 data of RCP4.5 and RCP8.5 scenarios are considered here to estimate the change in ET in the future for the decades of the 2020s, 2030s, 2040s, and 2050s (Figures 8 and 9). The mean of 10 years of data is presented in these decades for three stations, i.e., Betul, Hoshangabad, and Raisen. Increased maximum and minimum temperature are projected in the future in all stations in the RCP4.5 and RCP8.5. The annual maximum temperature of Betul in 2011 was 32.30 °C, which increases in 2050 to 33.58 °C in RCP4.5 and 35.01 °C in RCP8.5. The annual minimum temperature is also projected to increase from 20.30 °C to 21.75 °C and 23.07 °C in RCP4.5 and RCP8.5, respectively, in 2050. In Hoshangabad, the annual maximum temperature of 33.32 °C in 2011 increases to 34.59 °C and 35.94 °C in RCP4.5 and RCP8.5 scenarios, respectively, in 2050. The minimum temperature increases from 20.40 °C in 2011 to about 21.87 °C and 23.19 °C, respectively, in 2050. In Raisen, the annual maximum temperature of 33.49 °C in 2011 increases to 34.64 °C in RCP4.5 and 35.99 °C in RCP8.5 in 2050. The annual minimum temperature increases from 20.59 °C to 21.97 °C in RCP4.5 and 23.32 °C in RCP8.5 in 2050. In all the stations during the premonsoon or dry summer season, a considerably higher projection of maximum temperature is indicated. The monsoon season projects a low rate of increase as this is a season of continuous rainfall and overcast sky. The postmonsoon season and winter also indicate increased maximum temperature in the future in both RCP4.5 and RCP8.5 scenarios. Minimum temperature shows a higher increase rate of both premonsoon and monsoon temperature than in other seasons.

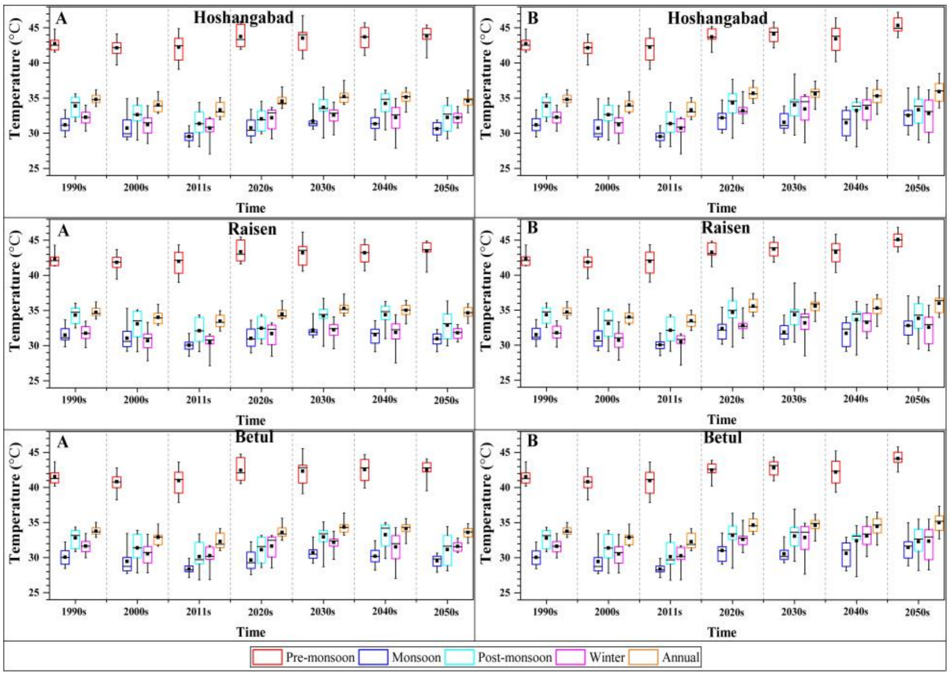

Figure 8. Maximum temperature of past and future (1990s to 2050s) using ACCESS1 of CMIP5 and scenarios are A = RCP4.5 and B = RCP8.5.

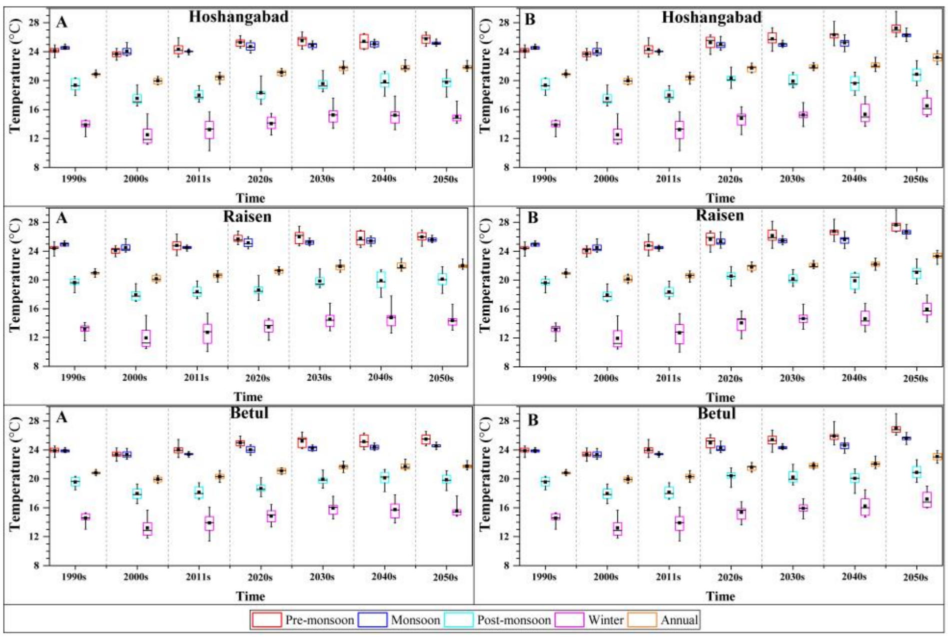

Figure 9. Minimum temperature of past and future (1990s to 2050s) using ACCESS1 of CMIP5 and scenarios are A = RCP4.5 and B = RCP8.5.

4.5. Impact of Future Climate and Land Use Changes on ET

4.5.1. Future Change of Seasonal and Annual ET Due to Land Use Change

The actual ET in different seasons for past, present, and future is given in Figure 10. The results show that the ET is decreasing in the future due to the land use change from 1990 to 2050. The 1990 ET is the highest, and 2050 projects the lowest ET in the future in all the seasons. This is due to the removal of forest and vegetation cover and conversion of these lands to other classes (from 981.06 mm in 1990 to 841.56 mm annually in 2050). According to the future land use prediction in 2050, forest and vegetated lands are decreasing at a higher rate and are converted to agricultural land and settlements. Therefore, ET will be decreasing in the future because of the changed land use. The premonsoon season shows the highest ET in all the years in the past, present, and in the future with a decrease of about 348.54 mm in 1990 annually to 316.53 mm in 2050. The monsoon season shows the highest ET after the premonsoon season in all the years and in the future. Annual ET varies from 298.58 mm in 1990 to 223.57 mm in 2050. The winter season shows a slight increase in annual ET in the future varying from 183.16 mm in 1990 to 189.73 mm in 2050.

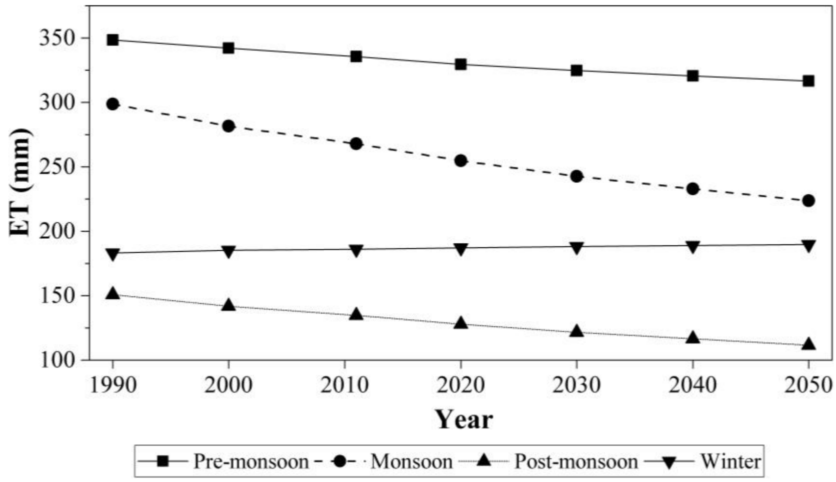

Figure 10. Land use change impact on ET.

4.5.2. Future Change of Seasonal and Annual ET Due to Climate Change

The change in the ET with climate change in different seasons from the 1990s to 2050s is given in Figure 11. ET is increasing in the future due to the effects of climate change. In the 1990s in the RCP4.5 scenario, annual ET is 941.42 mm, projected to increase to 950.93 mm in the 2050s. In the RCP8.5 scenario, it increases to 976.72 mm in the 2050s. An increased ET is projected in the premonsoon, monsoon, and winter seasons of RCP4.5 and in all the seasons of RCP8.5. The temperature is projected to increase in the future, which results in an increased projected ET from the 1990s to 2050s. The ET increase in the premonsoon season is highest in the RCP4.5 and both the premonsoon and monsoon seasons in RCP8.5. In the premonsoon season, the increase is projected from 334.17 mm in the 1990s to 341.07 mm in RCP4.5 and 348.09 mm in RCP8.5 in the 2050s. In the monsoon season of RCP8.5, the ET is projected to increase from 274.78 mm in the 1990s to 287.94 mm in the 2050s.

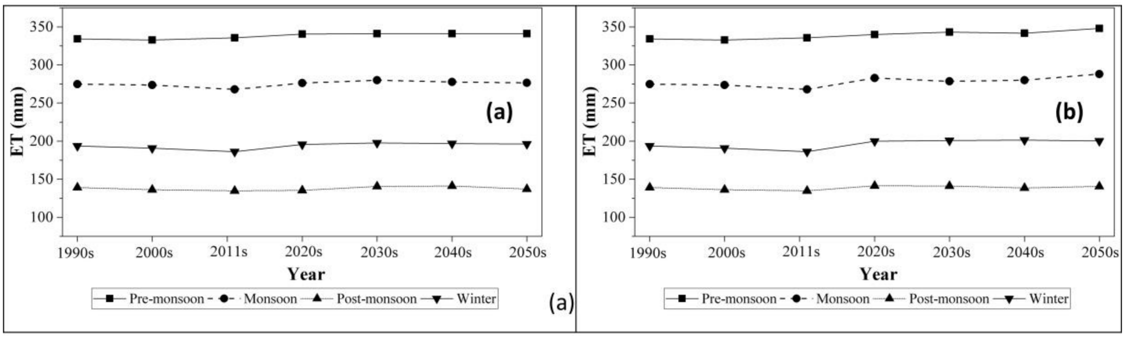

Figure 11. Climate change impact on ET (**a**) RCP4.5; (**b**) RCP8.5.

4.5.3. Future Change of Seasonal and Annual ET Due to Climate and Land Use Changes

The combined effects of climate and land use changes on ET is illustrated in Figure 12. The results show a decrease in the projected ET from 1990 to 2050 annually and in most of the seasons in both the RCP4.5 and RCP8.5 scenarios. The land use change and climate change of RCP4.5 projects a decrease in the annual ET from 1990 (997.63 mm) to 2050 (868.36 mm). The RCP8.5 scenario shows a decrease to 893.48 mm in 2050. All the premonsoon, monsoon, and postmonsoon seasons indicate a decrease in the ET, except the winter season. A slight increase is observed in the winter season ET due to combined land use and climate changes. However, as observed from the results, the effect of a change in land use will have more influence on the changed ET in the future than the effect of climate change.

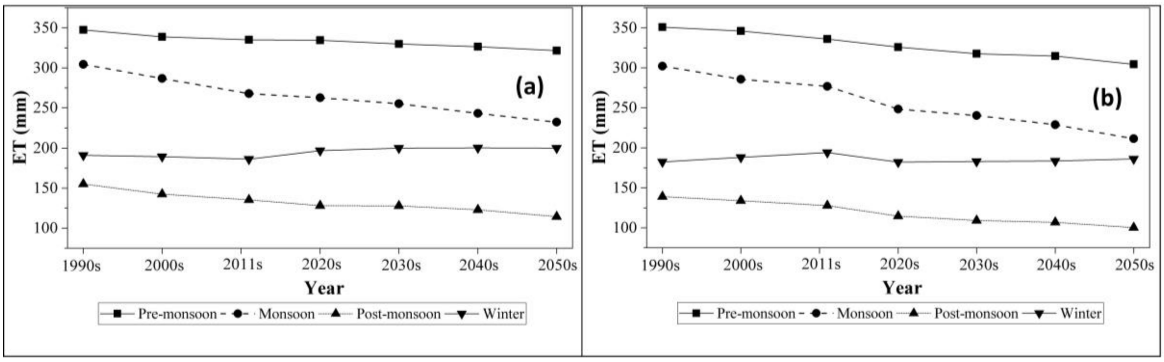

Figure 12. Climate and land use change impact on ET (**a**) RCP4.5; (**b**) RCP8.5.

5. Discussion and Conclusions

Evapotranspiration is one of the major factors in water balance and in various irrigation management systems. Therefore, appropriate information on spatial ET of a basin area is of utmost importance. Sufficient information on the spatial distribution of ET is not always available. No observed data on actual ET is available for this area. In the present study, the SEBAL method is applied to estimate the spatial actual ET for a basin area. The ET maps indicate high actual ET in the forest and other vegetated areas followed by the agricultural land. Water bodies show very high ET in all the images. Low ET is observed in agricultural fallow lands after the crop harvest. The premonsoon or summer time shows higher ET than other seasons because of the higher surface temperature. The winter season indicates higher ET because of crop-growing time during this season. A relationship of ET with the NDVI is observed, as higher ET is expected from healthy vegetation [75,80]. According to Mahmoud and Alazba [41], a gradual increase in monthly actual ET values is observed from January to April and a subsequent decline is observed from May to December in a part of Saudi Arabia. In this study, ET increases from winter to the premonsoon period and then decreases during the postmonsoon season, with varied types of land use. ET of the two main land use classes was 467.77 mm over the forest areas and 282.39 mm over agricultural areas during the premonsoon season, when ET is very high. During the growing season of winter, agricultural lands show 191.70 mm, while the harvest time of summer crops during the postmonsoon season shows very low ET (80.52 mm/winter season). Therefore, if the change in land use continues as it did from 1990 to 2011, increase in the agricultural land will cause even lower ET during the harvest time.

The impact of land use change has been observed to be dominant on the future actual ET of the basin area. A decrease is expected in ET in the future because of the conversion of vegetated land to other classes. SEBAL projects the lowest ET in 2050 in the future in comparison to the present ET in 2011 and past ET in 1990. Vegetation or forest has a higher fractional vegetation cover that results in a higher transpiration than the areas with low or medium fractional vegetation cover. Soil moisture also causes higher ET over agricultural and forest areas, while rocky surface areas are bare lands with high surface temperature and high sensible heat flux, resulting in low ET. It has been observed that there is no significant difference between the SEBAL-generated ET and the FAO Penman–Monteith method of daily ET estimation [13]. Du et al. [31] reported that ET of different land use and land cover increases from the vegetation up to June–July and then decreases, which conforms to the given results of increased ET in the premonsoon season and then decreased from September. The impact of climate change indicates an increase in the projected ET in the future in the three stations of the study area, which is due to increased projected temperature in the RCP4.5 and RCP8.5 scenarios. However, the combined impact of land use and climate change infers a decrease in the ET in the future. The effect of land use change here is more prominent than the climate change. The SEBAL model used to investigate climate change effects on crop evapotranspiration in Cyprus reported no significant changes [81]. Change in ET and runoff are observed due to land use and climate change, resulting in decreased ET in parts of Central India [82]. In a study in China, however, the impact of climate change is dominant, showing decreased ET due to a decrease in temperature and rainfall while increasing cropland shows higher ET [83]. Therefore, the effects of climate and land use changes may vary with local changes in the climate and land use characteristics. Uncertainties and limitations of the study are very essential as this is a new approach to estimate the future ET with respect to land use and climate change. There are scopes to evolve and develop this method by considering many factors and different research questions. To estimate ET from SEBAL, an average of three years of MODIS data was used here to obtain ET values of different land use classes. The use of more data will provide a sounder base of ET values for different land use classes. Monsoon data was not available for all the three years, which inhibits proper estimation of the changes in ET during this season. The impact of future climate change on ET was estimated by changing the minimum and maximum temperature, keeping all other parameters in the SEBAL model as constant. Changing other parameters in SEBAL requires generating different climate parameters in the future, which can be used as a future scope to this study. Seasonal variation in the land use changes and alternative climate and land use change scenarios can also be considered as a future scope. Agricultural lands vary with different crop cover, which will give different actual ET and which can be used for future research.

Supplementary Materials: The detailed processes followed in obtaining the results are available online at http://www.mdpi.com/2072-4292/10/4/578/s1.

Acknowledgments: The authors are thankful to the Indian Meteorological Department (IMD) for the weather data, Trade and Industry of Japan (METI) and the National Aeronautics and Space Administration (NASA) for the satellite data, and climate data from Coordinated Regional Climate Downscaling Experiment (CORDEX). The authors also express sincere thanks to the University Grant Commission (UGC) for financial assistance. Sincere thanks also extended to Hyunglok Kim for his help.

Author Contributions: All the authors have significant contributions to this research. Sananda Kundu, Arun Mondal, and Deepak Khare designed the research and analyzed, Christopher Hain and Venkat Lakshmi reviewed, advised, and contributed in improving the design of the paper.

Conflicts of Interest: The authors declare no conflict of interest.

References

1. Bouwer, L.M.; Biggs, T.W.; Aerts, J.C. Estimates of spatial variation in evaporation using satellite-derived surface temperature and a water balance model. *Hydrol. Process.* **2008**, *22*, 670–682. [CrossRef]
2. Bergez, J.-E.; Garcia, F.; Lapasse, L. A hierarchical partitioning method for optimizing irrigation strategies. *Agric. Syst.* **2004**, *80*, 235–253. [CrossRef]
3. Gowda, P.H.; Chavez, J.L.; Colaizzi, P.D.; Evett, S.R.; Howell, T.A.; Tolk, J.A. ET mapping for agricultural water management: Present status and challenges. *Irrig. Sci.* **2008**, *26*, 223–237. [CrossRef]
4. Intergovernmental Panel on Climate Change (IPCC). Working Group II: Impacts, Adaptation and Vulnerability. 2000. Available online: http://www.ipcc.ch/ipccreports/tar/wg2/index.php?idp=29 (accessed on 2 April 2018).
5. Shukla, J.; Mintz, Y. Influence of land-surface evapotranspiration on the earth's climate. *Science* **1982**, *215*, 1498–1501. [CrossRef] [PubMed]
6. Seneviratne, S.I.; Koster, R.D.; Guo, Z.; Dirmeyer, P.A.; Kowalczyk, E.; Lawrence, D.; Liu, P.; Mocko, D.; Lu, C.H.; Oleson, K.W.; et al. Soil moisture memory in AGCM simulations: Analysis of global land–atmosphere coupling experiment (GLACE) data. *J. Hydrometeorol.* **2006**, *7*, 1090–1112. [CrossRef]
7. Vicente-Serrano, S.M.; Azorin-Molina, C.; Sanchez-Lorenzo, A.; Revuelto, J.; López-Moreno, J.I.; González-Hidalgo, J.C.; Moran-Tejeda, E.; Espejo, F. Reference evapotranspiration variability and trends in Spain, 1961–2011. *Glob. Planet. Chang.* **2014**, *121*, 26–40. [CrossRef]
8. Wiesner, C.J. *Climate, Irrigation and Agriculture*; Angus and Robertson: Sydney, Australia, 1970.
9. Hassan, Q.K.; Bourque, C.P.-A.; Meng, F.-R.; Cox, R.M. A wetness index using terrain-corrected surface temperature and normalized difference vegetation index derived from standard MODIS products: An evaluation of its use in a humid forest-dominated region of eastern Canada. *Sensors* **2007**, *7*, 2028–2048. [CrossRef] [PubMed]
10. King, D.A.; Bachelet, D.M.; Symstad, A.J.; Ferschweiler, K.; Hobbins, M. Estimation of potential evapotranspiration from extraterrestrial radiation, air temperature and humidity to assess future climate change effects on the vegetation of the Northern Great Plains, USA. *Ecol. Model.* **2015**, *297*, 86–97. [CrossRef]
11. Stroeve, J.C.; Box, J.E.; Haran, T. Evaluation of the MODIS (MOD10A1) daily snow albedo product over the Greenland ice sheet. *Remote Sens. Environ.* **2006**, *105*, 155–171. [CrossRef]
12. Huo, Z.; Dai, X.; Feng, S.; Kang, S.; Huang, G. Effect of climate change on reference evapotranspiration and aridity index in arid region of China. *J. Hydrol.* **2013**, *492*, 24–34. [CrossRef]
13. Rahimi, S.; Sefidkouhi, M.A.G.; Raeini-Sarjaz, M.; Valipour, M. Estimation of actual evapotranspiration by using MODIS images (a case study: Tajan catchment). *Arch. Agron. Soil Sci.* **2015**, *61*, 695–709. [CrossRef]
14. Tang, R.; Li, Z.-L.; Sun, X. Temporal upscaling of instantaneous evapotranspiration: An intercomparison of four methods using eddy covariance measurements and MODIS data. *Remote Sens. Environ.* **2013**, *138*, 102–118. [CrossRef]
15. Wild, M.; Folini, D.; Schär, C.; Loeb, N.; Dutton, E.G.; König-Langlo, G. The global energy balance from a surface perspective. *Clim. Dyn.* **2013**, *40*, 3107–3134. [CrossRef]
16. Droogers, P.; Bastiaanssen, W. Irrigation performance using hydrological and remote sensing modeling. *J. Irrig. Drain. Eng.* **2002**, *128*, 11–18. [CrossRef]
17. Bastiaanssen, W.; Noordman, E.; Pelgrum, H.; Davids, G.; Thoreson, B.; Allen, R. Sebal model with remotely sensed data to improve water-resources management under actual field conditions. *J. Irrig. Drain. Eng.* **2005**, *131*, 85–93. [CrossRef]
18. Allen, R.G.; Tasumi, M.; Trezza, R. Satellite-based energy balance for mapping evapotranspiration with internalized calibration (metric)—Model. *J. Irrig. Drain. Eng.* **2007**, *133*, 380–394. [CrossRef]
19. Laymon, C.; Quattrochi, D.; Malek, E.; Hipps, L.; Boettinger, J.; McCurdy, G. Remotely-sensed regional-scale evapotranspiration of a semi-arid Great Basin Desert and its relationship to geomorphology, soils, and vegetation. *Geomorphology* **1998**, *21*, 329–349. [CrossRef]
20. Morse, A.; Tasumi, M.; Allen, R.G.; Kramber, W.J. *Application of the SEBAL Methodology for Estimating Consumptive Use of Water and Streamflow Depletion in the Bear River Basin of Idaho through Remote Sensing*; Idaho Department of Water Resources: Boise, ID, USA; University of Idaho, ID, USA, 2000.

21. Batra, N.; Islam, S.; Venturini, V.; Bisht, G.; Jiang, L. Estimation and comparison of evapotranspiration from MODIS and AVHRR sensors for clear sky days over the southern great plains. *Remote Sens. Environ.* **2006**, *103*, 1–15. [CrossRef]
22. McCabe, M.F.; Wood, E.F. Scale influences on the remote estimation of evapotranspiration using multiple satellite sensors. *Remote Sens. Environ.* **2006**, *105*, 271–285. [CrossRef]
23. Zhang, X.; Sun, R.; Zhang, B.; Tong, Q. Land cover classification of the north China plain using MODIS-EVI time series. *ISPRS J. Photogramm. Remote Sens.* **2008**, *63*, 476–484. [CrossRef]
24. Kiptala, J.; Mohamed, Y.; Mul, M.L.; Zaag, P. Mapping evapotranspiration trends using MODIS and SEBAL model in a data-scarce and heterogeneous landscape in eastern Africa. *Water Resour. Res.* **2013**, *49*, 8495–8510. [CrossRef]
25. Sun, Z.; Gebremichael, M.; Ardö, J.; Nickless, A.; Caquet, B.; Merboldh, L.; Kutschi, W. Estimation of daily evapotranspiration over Africa using MODIS/TERRA and SEVIRI/MSG data. *Atmos. Res.* **2012**, *112*, 35–44. [CrossRef]
26. Cammalleri, C.; Anderson, M.; Gao, F.; Hain, C.; Kustas, W. A data fusion approach for mapping daily evapotranspiration at the field scale. *Water Resour. Res.* **2013**, *49*, 4672–4686. [CrossRef]
27. Cammalleri, C.; Anderson, M.; Gao, F.; Hain, C.; Kustas, W. Mapping daily evapotranspiration at field scales over rainfed and irrigated agricultural areas using remote sensing data fusion. *Agric. For. Meteorol.* **2014**, *186*, 1–11. [CrossRef]
28. Bastiaanssen, W.G.; Menenti, M.; Feddes, R.; Holtslag, A. A remote sensing surface energy balance algorithm for land (SEBAL). 1. Formulation. *J. Hydrol.* **1998**, *212*, 198–212. [CrossRef]
29. Bastiaanssen, W.G.; Pelgrum, H.; Wang, J.; Ma, Y.; Moreno, J.; Roerink, G.; Van der Wal, T. A remote sensing surface energy balance algorithm for land (SEBAL): Part 2: Validation. *J. Hydrol.* **1998**, *212*, 213–229. [CrossRef]
30. Sun, Z.; Wei, B.; Su, W.; Shen, W.; Wang, C.; You, D.; Liu, Z. Evapotranspiration estimation based on the SEBAL model in the Nansi lake wetland of China. *Math. Comput. Model.* **2011**, *54*, 1086–1092. [CrossRef]
31. Du, J.; Song, K.; Wang, Z.; Zhang, B.; Liu, D. Evapotranspiration estimation based on MODIS products and surface energy balance algorithms for land (SEBAL) model in Sanjiang plain, northeast china. *Chin. Geogr. Sci.* **2013**, *23*, 73–91. [CrossRef]
32. Bastiaanssen, W.; Pelgrum, H.; Soppe, R.; Allen, R.; Thoreson, B.; de C. Teixeira, A. Thermal-infrared technology for local and regional scale irrigation analyses in horticultural systems. *ActaHortic* **2008**, *792*, 33–46.
33. Papadavid, G.; Hadjimitsis, D.G.; Toulios, L.; Michaelides, S. A modified sebal modeling approach for estimating crop evapotranspiration in semi-arid conditions. *Water Resour. Manag.* **2013**, *27*, 3493–3506. [CrossRef]
34. Bashir, M.; Hata, T.; Tanakamaru, H.; Abdelhadi, A.; Tada, A. Satellite-based energy balance model to estimate seasonal evapotranspiration for irrigated sorghum: A case study from the Gezira scheme, Sudan. *Hydrol. Earth Syst. Sci.* **2008**, *12*, 1129–1139. [CrossRef]
35. Abrishamkar, M.; Ahmadi, A. Evapotranspiration estimation using remote sensing technology based on SEBAL algorithm. *Iran. J. Sci. Technol. Trans. Civ. Eng.* **2017**, *41*, 65–76. [CrossRef]
36. Ahmad, M.-D.; Biggs, T.; Turral, H.; Scott, C.A. Application of SEBAL approach and modis time-series to map vegetation water use patterns in the data scarce Krishna river basin of India. *Water Sci. Technol.* **2006**, *53*, 83–90. [CrossRef] [PubMed]
37. Bala, A.; Rawat, K.S.; Misra, A.K.; Srivastava, A. Assessment and validation of evapotranspiration using SEBAL algorithm and lysimeter data of IARI agricultural farm, India. *Geocarto Int.* **2016**, *31*, 739–764. [CrossRef]
38. Parmar, H.; Gontia, N. Irrigation water management modeling in canal command using remote sensing. *Ann. Arid Zone* **2016**, *55*, 89–99.
39. Jana, C.; Rawat, M.; Sena, D.R.; Alam, N.M.; Mandal, U.; Kaushal, R.; Mishra, P.K. Application of SEBAL model to estimate Evapotranspiration in Doon Valley, India. *Indian J. Soil Conserv.* **2016**, *44*, 191–197.
40. Cai, X.; Sharma, B.R. Integrating remote sensing, census and weather data for an assessment of rice yield, water consumption and water productivity in the Indo-Gangetic river basin. *Agric. Water Manag.* **2010**, *97*, 309–316. [CrossRef]

41. Mahmoud, S.H.; Alazba, A. A coupled remote sensing and the surface energy balance based algorithms to estimate actual evapotranspiration over the western and southern regions of Saudi Arabia. *J. Asian Earth Sci.* **2016**, *124*, 269–283. [CrossRef]
42. Bastiaanssen, W. SEBAL-based sensible and latent heat fluxes in the irrigated Gediz basin, turkey. *J. Hydrol.* **2000**, *229*, 87–100. [CrossRef]
43. Timmermans, W.J.; Kustas, W.P.; Anderson, M.C.; French, A.N. An intercomparison of the surface energy balance algorithm for land (SEBAL) and the two-source energy balance (TSEB) modeling schemes. *Remote Sens. Environ.* **2007**, *108*, 369–384. [CrossRef]
44. Minacapilli, M.; Agnese, C.; Blanda, F.; Cammalleri, C.; Ciraolo, G.; D'Urso, G.; Iovino, M.; Pumo, D.; Provenzano, G.; Rallo, G. Estimation of actual evapotranspiration of Mediterranean perennial crops by means of remote-sensing based surface energy balance models. *Hydrol. Earth Syst. Sci.* **2009**, *13*, 1061–1074. [CrossRef]
45. Yang, J.-Y.; Mei, X.-R.; Huo, Z.-G.; Yan, C.-R.; Hui, J.; Zhao, F.-H.; Qin, L. Water consumption in summer maize and winter wheat cropping system based on SEBAL model in Huang-Huai-Hai plain, China. *J. Integr. Agric.* **2015**, *14*, 2065–2076. [CrossRef]
46. Wu, B.; Zhu, W.; Yan, N.; Feng, X.; Xing, Q.; Zhuang, Q. An improved method for deriving daily evapotranspiration estimates from satellite estimates on cloud-free days. *IEEE J. Sel. Top. Appl. Earth Obs. Remote Sens.* **2016**, *9*, 1323–1330. [CrossRef]
47. Luo, T.; Jutla, A.; Islam, S. Evapotranspiration estimation over agricultural plains using MODIS data for all sky conditions. *Int. J. Remote Sens.* **2015**, *36*, 1235–1252. [CrossRef]
48. Steele, D.D.; Thoreson, B.P.; Hopkins, D.G.; Clark, B.A.; Tuscherer, S.R.; Gautam, R. Spatial mapping of evapotranspiration over Devils lake basin with SEBAL: Application to flood mitigation via irrigation of agricultural crops. *Irrig. Sci.* **2015**, *33*, 15–29. [CrossRef]
49. Senay, G.B.; Friedrichs, M.; Singh, R.K.; Velpuri, N.M. Evaluating landsat 8 evapotranspiration for water use mapping in the colorado river basin. *Remote Sens. Environ.* **2016**, *185*, 171–185. [CrossRef]
50. Jiménez-Bello, M.Á.; Castel, J.R.; Testi, L.; Intrigliolo, D.S. Assessment of a remote sensing energy balance methodology (SEBAL) using different interpolation methods to determine evapotranspiration in a citrus orchard. *IEEE J. Sel. Top. Appl. Earth Obs. Remote Sens.* **2015**, *8*, 1465–1477. [CrossRef]
51. Bhattarai, N.; Shaw, S.B.; Quackenbush, L.J.; Im, J.; Niraula, R. Evaluating five remote sensing based single-source surface energy balance models for estimating daily evapotranspiration in a humid subtropical climate. *Int. J. Appl. Earth Obs. Geoinform.* **2016**, *49*, 75–86. [CrossRef]
52. Tang, R.; Li, Z.-L. Evaluation of two end-member-based models for regional land surface evapotranspiration estimation from MODIS data. *Agric. For. Meteorol.* **2015**, *202*, 69–82. [CrossRef]
53. Lian, J.; Huang, M. Comparison of three remote sensing based models to estimate evapotranspiration in an oasis-desert region. *Agric. Water Manag.* **2016**, *165*, 153–162. [CrossRef]
54. Sharma, V.; Kilic, A.; Irmak, S. Impact of scale/resolution on evapotranspiration from Landsat and MODIS images. *Water Resour. Res.* **2016**, *52*, 1800–1819. [CrossRef]
55. Wang, Y.Q.; Xiong, Y.J.; Qiu, G.Y.; Zhang, Q.T. Is scale really a challenge in evapotranspiration estimation? A multi-scale study in the Heihe oasis using thermal remote sensing and the three-temperature model. *Agric. For. Meteorol.* **2016**, *230*, 128–141. [CrossRef]
56. Zheng, C.; Wang, Q.; Li, P. Coupling SEBAL with a new radiation module and MODIS products for better estimation of evapotranspiration. *Hydrol. Sci. J.* **2016**, *61*, 1535–1547. [CrossRef]
57. Liaqat, U.W.; Choi, M. Accuracy comparison of remotely sensed evapotranspiration products and their associated water stress footprints under different land cover types in Korean peninsula. *J. Clean. Prod.* **2016**, *155*, 93–104. [CrossRef]
58. Alidoost, F.; Sharifi, M.A.; Stein, A. Region-and pixel-based image fusion for disaggregation of actual evapotranspiration. *Int. J. Image Data Fusion* **2015**, *6*, 216–231. [CrossRef]
59. Allen, R.G.; Pereira, L.S.; Raes, D.; Smith, M. *Crop Evapotranspiration-Guidelines for Computing Crop Water Requirements-FAO Irrigation and Drainage Paper 56*; FAO: Rome, Italy, 1998; Volume 300, p. D05109.
60. Bastiaanssen, W.G.M. Regionalization of surface flux densities and moisture indicators in composite terrain. In a Remote Sensing Approach under Clear Skies in Mediterranean Climates; 1995. Available online: http://library.wur.nl/WebQuery/wda/918192 (accessed on 10 May 2012).

61. Goetz, S. Multi-sensor analysis of NDVI, surface temperature and biophysical variables at a mixed grassland site. *Int. J. Remote Sens.* **1997**, *18*, 71–94. [CrossRef]
62. Allen, R.; Tasumi, M.; Trezza, R.; Waters, R.; Bastiaanssen, W. Sebal (surface energy balance algorithms for land). In Advance Training and Users Manual–Idaho Implementation, Version, 2002; Volume 1, p. 97. Available online: https://www.researchgate.net/file.PostFileLoader.html?id=5635f25060614b180d8b4567&assetKey=AS%3A290936253894656%401446376016229 (accessed on 8 May 2012).
63. Wu, Q.; Li, H.-Q.; Wang, R.-S.; Paulussen, J.; He, Y.; Wang, M.; Wang, B.-H.; Wang, Z. Monitoring and predicting land use change in Beijing using remote sensing and GIS. *Landsc. Urban Plan.* **2006**, *78*, 322–333. [CrossRef]
64. Mukhopadhyay, A.; Mondal, A.; Mukherjee, S.; Khatua, D.; Ghosh, S.; Mitra, D.; Ghosh, T. Forest cover change prediction using hybrid methodology of geoinformatics and markov chain model: A case study on sub-himalayan town Gangtok, India. *J. Earth Syst. Sci.* **2014**, *123*, 1349–1360. [CrossRef]
65. Mondal, A.; Khare, D.; Kundu, S.; Mishra, P.; Meena, P. Landuse Change Prediction and Its Impact on surface Run-Off Using Fuzzy C-Mean, Markov Chain and Curve Number Methods. In Proceedings of the Third International Conference on Soft Computing for Problem; Springer: Berlin, Germany, 2014; pp. 365–376. Available online: https://doi.org/10.1007/978-81-322-1768-8_33 (accessed on 5 March 2014)
66. Chen, C.-F.; Son, N.-T.; Chang, N.-B.; Chen, C.-R.; Chang, L.-Y.; Valdez, M.; Centeno, G.; Thompson, C.A.; Aceituno, J.L. Multi-decadal mangrove forest change detection and prediction in Honduras, central America, with Landsat imagery and a Markov chain model. *Remote Sens.* **2013**, *5*, 6408–6426. [CrossRef]
67. Alqurashi, A.F.; Kumar, L.; Sinha, P. Urban land cover change modelling using time-series satellite images: A case study of urban growth in five cities of Saudi Arabia. *Remote Sens.* **2016**, *8*, 838. [CrossRef]
68. Athmania, D.; Achour, H. External validation of the Aster GDEM2, gmted2010 and CGIAR-CSI-SRTM v4. 1 free access digital elevation models (DEMs) in Tunisia and Algeria. *Remote Sens.* **2014**, *6*, 4600–4620. [CrossRef]
69. Scott, A.J.; Symons, M.J. Clustering methods based on likelihood ratio criteria. *Biometrics* **1971**, *27*, 387–397. [CrossRef]
70. Wang, G.; He, G.; Liu, J. A New Classification Method for High Spatial Resolution Remote Sensing Image Based on Mapping Mechanism. In Proceedings of the International Conference on Geographic Object-Based Image Analysis (GEOBIA'12), Rio de Janeiro, Brazil, 7–9 May 2012; pp. 186–190.
71. Weng, Q. Land use change analysis in the Zhujiang delta of china using satellite remote sensing, GIS and stochastic modelling. *J. Environ. Manag.* **2002**, *64*, 273–284. [CrossRef]
72. Sanjay, J.; Krishnan, R.; Shrestha, A.B.; Rajbhandari, R.; Ren, G.Y. Downscaled climate change projections for the Hindu Kush Himalayan region using CORDEX South Asia regional climate models. *Adv. Clim. Chang. Res.* **2017**, *8*, 185–198. [CrossRef]
73. Carlson, T.N.; Perry, E.M.; Schmugge, T.J. Remote estimation of soil moisture availability and fractional vegetation cover for agricultural fields. *Agric. For. Meteorol.* **1990**, *52*, 45–69. [CrossRef]
74. Kalluri, S.N.; Townshend, J.R.; Doraiswamy, P. A simple single layer model to estimate transpiration from vegetation using multi-spectral and meteorological data. *Int. J. Remote Sens.* **1998**, *19*, 1037–1053. [CrossRef]
75. Bindhu, V.M.; Narasimhan, B.; Sudheer, K.P. Development and verification of a non-linear disaggregation method (NL-DisTrad) to downscale MODIS land surface temperature to the spatial scale of Landsat thermal data to estimate evapotranspiration. *Remote Sens. Environ.* **2013**, *135*, 118–129. [CrossRef]
76. Kumar, D.; Shekhar, S. Statistical analysis of land surface temperature–vegetation indexes relationship through thermal remote sensing. *Ecotoxicol. Environ. Saf.* **2015**, *121*, 39–44. [CrossRef] [PubMed]
77. Guo, G.; Wu, Z.; Xiao, R.; Chen, Y.; Liu, X.; Zhang, X. Impacts of urban biophysical composition on land surface temperature in urban heat island clusters. *Landsc. Urban Plan.* **2015**, *135*, 1–10. [CrossRef]
78. Tran, D.X.; Pla, F.; Latorre-Carmona, P.; Myint, S.W.; Caetano, M.; Kieu, H.V. Characterizing the relationship between land use land cover change and land surface temperature. *ISPRS J. Photogramm. Remote Sens.* **2017**, *124*, 119–132. [CrossRef]
79. Landis, J.R.; Koch, G.G. The measurement of observer agreement for categorical data. *Biometrics* **1977**, *33*, 159–174. [CrossRef] [PubMed]
80. Milich, L.; Weiss, E. Gac NDVI images: Relationship to rainfall and potential evaporation in the grazing lands of the Gourma (Northern Sahel) and in the croplands of the Niger-Nigeria border (Southern Sahel). *Int. J. Remote Sens.* **2000**, *21*, 261–280. [CrossRef]

81. Papadavid, G.; Neocleous, D.; Kountios, G.; Markou, M.; Michailidis, A.; Ragkos, A.; Hadjimitsis, D. Using SEBAL to Investigate How Variations in Climate Impact on Crop Evapotranspiration. *J. Imaging* **2017**, *3*. [CrossRef]
82. Kundu, S.; Khare, D.; Mondal, A. Individual and combined impacts of future climate and land use changes on the water balance. *Ecol. Eng.* **2017**, *105*, 42–57. [CrossRef]
83. Yuan, X.; Bai, J.; Li, L.; Kurban, A.; De Maeyer, P. The dominant role of climate change in determining changes in evapotranspiration in Xinjiang, China from 2001 to 2012. *PLoS ONE* **2017**, *12*, e0183071. [CrossRef] [PubMed]